IAA-ICSSA-17-0X-XX
DRAG DE-ORBIT DEVICE: A NEW STANDARD RE-ENTRY ACTUATOR FOR CUBESATS

David Guglielmo[(1)], **Sanny Omar**[(2)], **Riccardo Bevilacqua**[(3)]
[(1)]*Postdoctoral Researcher, MAE-A 211, 939 Sweet Water Drive, Gainesville, FL 32611, 352-846-1477, dguglielmo@ufl.edu*
[(2)]*Graduate Researcher, MAE-A 211, 939 Sweet Water Drive, Gainesville, FL 32611, 352-846-1477, sanny.omar@ufl.edu*
[(3)]*Associate Professor, MAE-A 211, 939 Sweet Water Drive, Gainesville, FL 32611, 352-846-1477, bevilr@ufl.edu*

Keywords: *Differential Drag, Targeted Re-Entry, Deorbit, ADACS, Attitude Stabilization*

With the advent of CubeSats, research in Low Earth Orbit (LEO) becomes possible for universities and small research groups. Only a handful of launch sites can be used, due to geographical and political restrictions. As a result, common orbits in LEO are becoming crowded due to the additional launches made possible by low-cost access to space. CubeSat design principles require a maximum of a 25-year orbital lifetime in an effort to reduce the total number of spacecraft in orbit at any time. Additionally, since debris may survive re-entry, it is ideal to de-orbit spacecraft over unpopulated areas to prevent casualties.

The Drag Deorbit Device (D3) is a self-contained targeted re-entry subsystem intended for CubeSats. By varying the cross-wind area, the atmospheric drag can be varied in such a way as to produce desired maneuvers. The D3 is intended to be used to remove spacecraft from orbit to reach a desired target interface point. Additionally, attitude stabilization is performed by the D3 prior to deployment and can replace a traditional ADACS on many missions.

This paper presents the hardware used in the D3 and operation details. Four stepper-driven, repeatedly retractable booms are used to modify the cross-wind area of the D3 and attached spacecraft. Five magnetorquers (solenoids) over three axes are used to damp rotational velocity. This system is expected to be used to improve mission flexibility and allow additional launches by reducing the orbital lifetime of spacecraft.

The D3 can be used to effect a re-entry to any target interface point, with the orbital inclination limiting the maximum latitude. In the chance that the main spacecraft fails, a timer will automatically deploy the booms fully, ensuring the spacecraft will

Email addresses: `dguglielmo@ufl.edu` (**David Guglielmo**), `sanny.omar@ufl.edu` (**Sanny Omar**), `bevilr@ufl.edu` (**Riccardo Bevilacqua**)

at the minimum reenter the atmosphere in the minimum possible time, although not necessarily at the desired target interface point. Although this does not reduce the risk of casualties, the 25-year lifetime limit is still respected, allowing a reduction of the risk associated with a hardware failure.

1. Introduction

As more and more spacecraft are launched, LEO (Low Earth Orbit) is becoming more crowded [1]. Many small spacecraft launch as secondary payloads and, if they have no propulsion systems, are constrained to operating in the orbit of the primary payload. CubeSats [2], small spacecraft primarily designed for university and research use, are a common example. Popular orbits such as sun-synchronous and space station orbits have become particularly crowded due to the increasing number of CubeSats being deployed into these orbits as secondary payloads [3].

The crowding of popular low Earth orbits has led to stricter regulations on orbital debris mitigation and the desire for improved orbital maneuvering capabilities to avoid collisions between satellites. To further reduce the chances of collision, small spacecraft are also required to de-orbit within 25 years, as per NASA-STD-8719.14A [4]. Spacecraft in high orbits can take hundreds of years to deorbit (depending on altitude), but they cannot remain operational indefinitely. After the operational lifetime of a spacecraft has elapsed, if it has not de-orbited, it becomes uncontrolled space debris. This can result in collisions between space objects, creating even more debris in a process known as Kessler Syndrome [5].

Spacecraft have traditionally been de-orbited with thrusters or drag in LEO. Using drag to de-orbit is a passive method, and can be expedited by the deployment of a large aerodynamic device. Various hardware configurations have been developed, such as the Terminator Tape™ [6] and Terminator Tether™ [7], De-orbit and Recovery System (DRS) [8], Gossamer Orbit Lowering Device (GOLD) [9], AEOLDOS [10], the iDOD [11], Deutsche Orbitale Servicing Mission (DEOS) [12], and drag sails [13, 14]. Increasing the drag sufficiently will decrease the orbit lifetime of a LEO spacecraft, but the eventual de-orbit location will be uncontrolled. NASA-STD-8719.14A mandates that any spacecraft utilizing controlled re-entry techniques must land 370 km away from land and that the probability of targeting failure multiplied by the chance of human casualty due to the uncontrolled re-entry be less than 1 in 10,000 [4]. Spacecraft containing thrusters can perform an impulsive de-orbit burn to ensure that their debris lands away from populated areas, as was the case with the Delta IV upper stages [15] and the Mir space station [16]. However, a failure of the propulsion system can result in uncontrolled re-entry and pose a significant hazard to persons or property on the ground, such as when Skylab fell over Australia in 1979 and generated a debris field in the Australian Outback [17].

Satellites without thrusters are severely limited in their ability to perform orbital maneuvering or controlled re-entry. However, differential drag techniques, or modifying the relative drag-induced acceleration between two spacecraft, have been proposed previously by Leonard in 1986 [18] as means of thruster-free orbital maneuvering, and then built upon by many researchers since then, including some of the authors of this paper [19, 20, 21]. By modulating the drag area of a spacecraft appropriately, the spacecraft can be made to de-orbit away from populated areas without the use of any thrusters [22]. This technique could be used to save fuel for spacecraft containing thrusters and could be used to provide controlled re-entry for spacecraft whose

2

thrusters have failed or that do not contain thrusters. The variation of atmospheric drag can be performed in several different ways including a rotation of the spacecraft panels [23] or the deployment of a drag device [24, 25]. Some of the authors of this paper have previously developed a repeatedly-retractable drag sail that can be modulated to produce changes in the satellite drag area [25].

Regardless of the method used, some measure of attitude control is necessary to maintain a predictable drag area for aerodynamically-based orbital maneuvering algorithms. COTS ADACS such as the BCT (Blue Canyon Technologies) XACT [26], MAI-400 (Maryland Aerospace, Inc.) [27] and a unit by ClydeSpace [28] are available for small spacecraft but can easily cost tens of thousands of dollars in addition to requiring significant mass and power onboard the host satellite.

This paper discusses the development of a retractable drag device for small spacecraft capable of modulating the drag area while providing 3-axis attitude stabilization using passive aerodynamic and gravity gradient torques and active damping using magnetorquers [29]. This Drag De-Orbit Device (D3) can be utilized for orbital maneuvering, collision avoidance, de-orbit point targeting for spacecraft containing components that may survive re-entry, and for passive, uncontrolled de-orbit for spacecraft that will disintegrate on re-entry. The system is unique in that it can provide simultaneous attitude stabilization and modulation of the spacecraft's drag area, a capability not shared by any commercially available drag devices. The simplicity and limited number of moving parts in the D3 system also make it a cheaper and more reliable alternative to conventional ADACS units for many satellite missions without strict pointing requirements. For example, a satellite needing to point an antenna and camera within 20 degrees of the nadir vector, maintain a desired separation between sister satellites in the same orbital plane, and de-orbit once its mission is complete could utilize the D3 exclusively as its attitude and orbit control system.

The D3 consists of four tape-spring booms; each is 3.7 m long when fully deployed, has a flat width of 4 cm, and is inclined at 20 degrees relative to the rear face of the satellite. The dart configuration of these booms causes the satellite to naturally ram-align due to aerodynamic forces. Partially retracting two of the booms opposite to each other results in a clear minimum moment of inertia axis which will simultaneously tend to align with the nadir vector due to gravity gradient torques, resulting in 3-axis attitude stabilization. Five magnetorquers are utilized with the B-dot detumble law to damp oscillations about the equilibrium attitude. Deploying or retracting all booms simultaneously varies the aerodynamic drag force experienced by the satellite while maintaining the aerodynamically stable ram-aligned attitude. A six degree of freedom attitude and orbit propagator [30] was developed to assess the attitude stability of the D3 system and make design decisions about the system geometry.

This paper begins with a summary of the D3 system objectives. The hardware design presented in Section 3 is geared toward the fulfillment of these objectives. The remainder of the paper discusses the operation of this hardware and the analysis and simulations conducted to refine and validate the hardware design. Section 4 discusses the modeling of the passive environmental forces and torques acting on the spacecraft that were taken into account in the 6-DOF orbit and attitude simulation. The proposed implementation of the popular B-Dot magnetorquer de-tumble law for active attitude rate damping is discussed in Section 5. Though many possible system configurations were tested using the simulation and control framework established up to this point, only the simulation results corresponding to the final system design are presented in

Section 6. These simulation results show that the system meets or exceeds the performance requirements. Section 7 includes thermal simulations conducted by the NASA Kennedy Space Center verifying that the proposed hardware will assume acceptable temperature profiles and results from repeated testing of the deployer. Section 8 details thermal vacuum and fatigue testing with the goal of assessing the performance of the device under harsh conditions. Finally, Section 9 presents the conclusions reached during the simulation and hardware design process.

2. System Requirements

In order to be used as a reliable, low-cost attitude and orbit control system on a variety of LEO CubeSats and potentially other small satellite missions, the D3 system is designed to meet the following requirements.

- The D3 shall weight less than 1.33 kg and occupy a volume of less than 1U (10 x 10 x 10 cm).

- The D3 shall integrate into a standard CubeSat structure and the external dimensions of the device shall conform to the CubeSat standard [2].

- The D3 must be able to successfully de-orbit a 12U, 15 kg spacecraft from 700 km circular orbit in under 25 years assuming standard atmospheric conditions.

- The D3 system must enable the spacecraft to maintain passive ram-alignment within 15 degrees up to an altitude of 700 km. This maximizes drag area in order to expedite de-orbit and provides a predictable drag profile for orbital maneuvering.

- The D3 must be fully retractable such that the aerodynamic profile of a CubeSat with the D3 retracted is identical to the profile of that CubeSat without the D3.

- Components of the D3 shall not create additional debris upon re-entry.

- All computing and control mechanisms required to operate the D3 shall be self-contained and capable of receiving commands from a CubeSat bus of compatible hardware.

- D3 peak power must remain under 20 W so that it can be controlled by an unmodified, commercially available CubeSat power system. Note that the D3 is not expected to use 20 W, but that this is a reasonable upper limit of what a commercial CubeSat power system could provide.

- Angular momentum should not be transferred to the spacecraft from the D3 system during deployment

- The system must be able to handle at least 500 cycles of deploying and retracting without experiencing fatigue-induced failures.
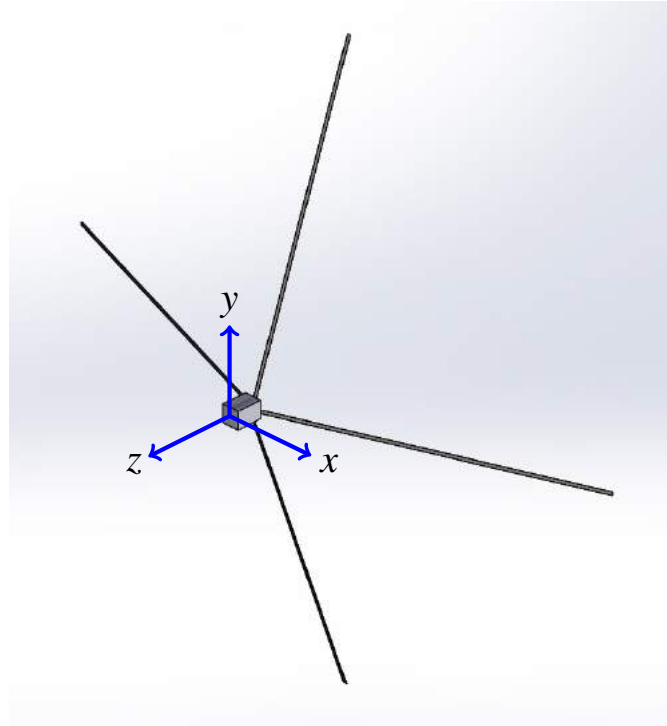
Figure 1: D3 Device Attached to a CubeSat with Body Axes Shown

3. D3 System Hardware

In keeping with the design requirements presented previously, the D3 system is designed with CubeSat compatibility in mind, although it is not restricted to CubeSat use. The maximum total projected cross-wind area is 0.5 m^2, which is sufficient to deorbit a 12U, 15 kg spacecraft in 25 years or less, and is further discussed in Section 6.1. Four independent booms are used to achieve this cross-wind area, which also provides attitude control and redundancy.

3.1. Booms Are Angled for Greater Stability

For aerodynamic stability, the booms are inclined at a 20 degree angle relative to the satellite face to which they are attached as shown in Fig. 1. As determined by simulations, increasing the angle would result in marginally more stability, at the cost of sharply increasing the required cross sectional area. Conversely, decreasing the angle results in a sharp decrease in stability with only a marginal increase in cross wind area. Since the D3 is intended to be used with a 12U CubeSat, the boom length is adjusted to achieve 0.5 m^2 past the cross wind area of the CubeSat. This results in a boom length of 3.7 m. Section 6 elaborates further on the attitude stability properties.

3.2. Fabrication of Booms

The booms are rolled from 0.003" (0.0762 mm) thick Austenitic 316 stainless steel stock. The initially flat stock is rolled into a rounded-V cross section to maintain its stiffness while in orbit. Using a two-roller, one-pass process, 3-point bending is used to achieve the desired geometry. The flat width of each piece is 40 mm but the cross wind width is approximately 38 mm after the boom is rolled. The roller geometry is shown in Fig. 2.
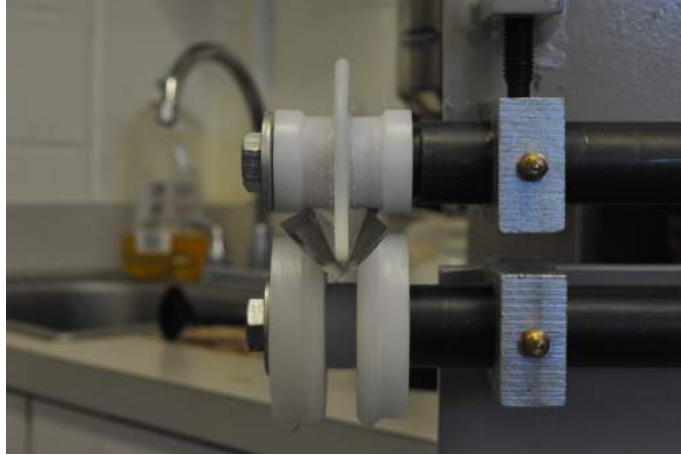
5

Figure 2: Bead Roller Geometry

Figure 3: Boom is Secured to Drum

Variation of the roller center-to-center distance is used to adjust the bend angle. Variation of the tip radius of curvature is used to adjust the radius of curvature of the rounded-V. Nylon was used for the rollers since different versions could be iterated rapidly. Because the Nylon rollers are much thicker than the stainless steel booms, any roller deformation during the rolling process will not be significant enough to affect the final boom geometry.

3.3. Assembly and Operation of a Boom Deployer

The deployer is constructed in a manner similar to a tape measure. Each boom is first attached to a drum with four screws as shown in Fig. 3, allowing rotation of the drum to deploy and retract the boom.

The drum is driven by a Faulhaber AM1524 stepper motor with an attached 81:1 gearbox [31]. The high reduction ratio ensures that the boom cannot backdrive the stepper, eliminating the need to power the motor when the booms are not being deployed or retracted, and allowing open-loop operation.

The motor is fastened inside a sleeve, the base of which is then fastened to the outer shell as shown in Figure 4. The drum is then fitted over the sleeve using a thrust roller bearing on each end to maintain alignment as shown in Fig. 5. Note that the drum contains a shoulder for mounting the bearing on the end closest to the gearbox

6

output shaft.

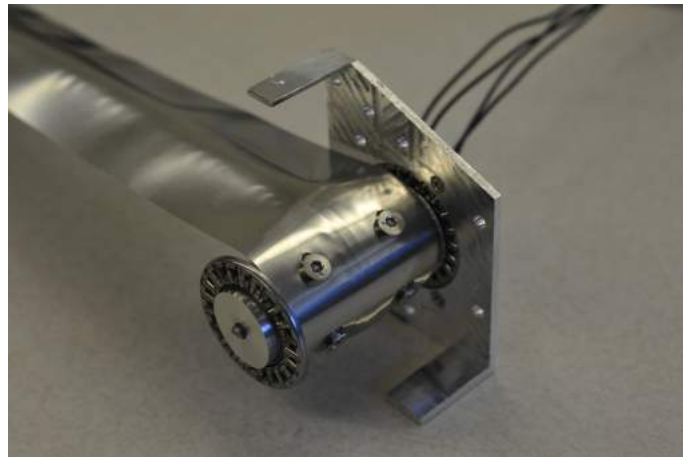**Figure 4: Sleeve Attaches To Motor for Later Mounting**

Figure 5: Drum is Placed Over Sleeve

A second shell is used to hold the deployer assembly together, with the bearing placed over the drum shoulder but inside a pocket in the shell. Four deployers are then attached to a base plate, spaced 90 degrees apart as shown in Fig. 6. An expanded view of each deployer is shown in Fig. 7.

3.4. Magnetorquer Design

For this system, the desired combined mass of all magnetorquers was approximately 100 g and it was assumed that the magnetorquers would be supplied by a 3.3 V CubeSat power system capable of supplying up to 15 W. The magnetorquers aligned with the x and y axes (Fig. 1) would be created by wrapping coils of wire around the screw heads on the D3 deployers while the z magnetorquer would be created by wrapping a coil of wire around the entire four-deployer assembly as shown in Figure 6. Because there are two deployer screw assemblies facing in the x-direction, the coils for the x-magnetorquer will be evenly distributed among both deployers. The same applies for the y-magnetorquer coils. The perimeter of each loop around the deployer screw heads is 170.3 mm and the area is 1951 mm^2. The perimeter of each loop of the z-magnetorquer is 380 mm and the area is 9025 mm^2. By using 160 turns of 25
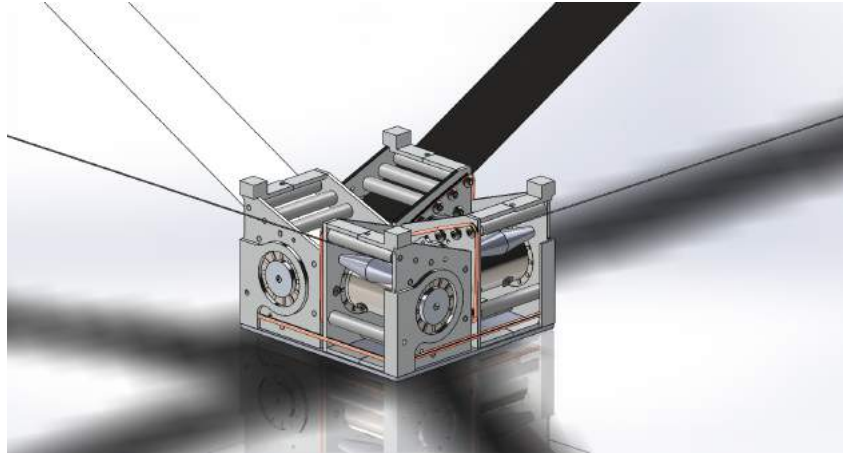
Figure 6: Four Deployers Are Mounted to the Base Plate
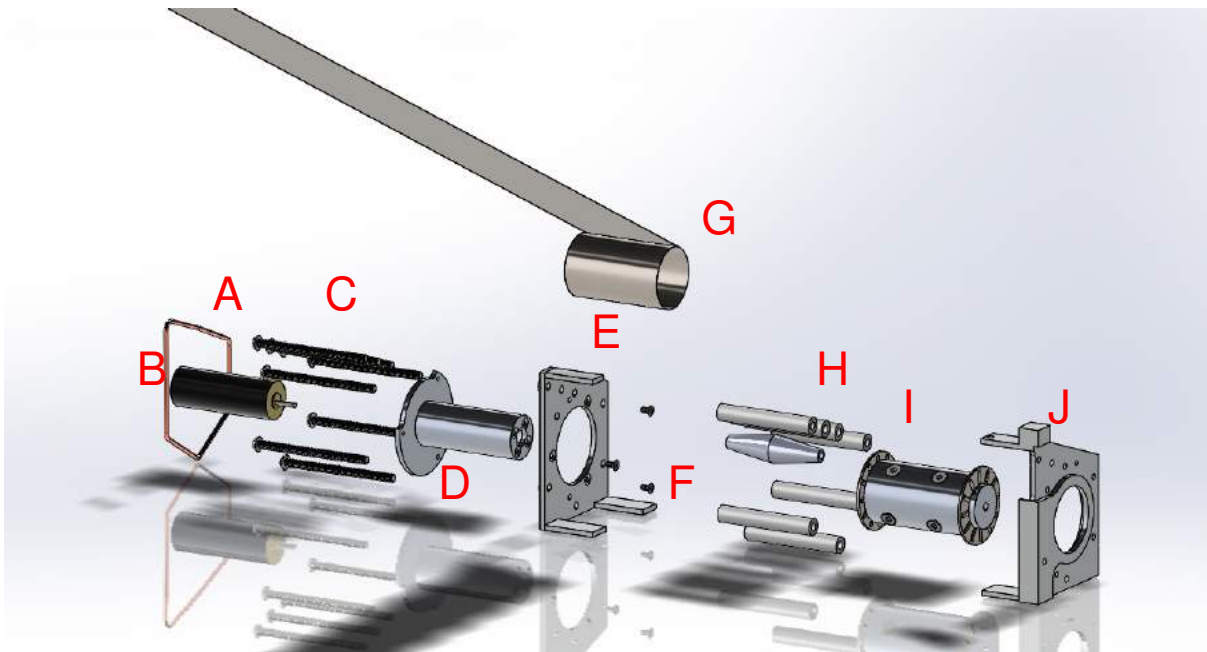

Figure 7: Assembly of a Single Deployer

American Wire Gauge (AWG) wire for the x and y magnetorquers and 40 turns for the z magnetorquer, the combined mass of the magnetorquers is 101 g, and the power consumption when 3.3 V is applied directly to all magnetorquers is 14.3 W. This magnetorquer design satisfies all the requirements and is capable of de-tumbling a 12U, 15 kg satellite in less than 18 hours with a maximum power consumption limited to 2 W, as discussed in Sec. 5.

3.5. D3 Hardware Control

The D3 system is controlled by a dedicated microcontroller. An OLinuXino Nano controller with iMX233 ARM926J processor at 454Mhz is used to independently control each deployer and magnetorquer. The hardware is open-source, and is integrated into a dedicated control board.

Four stepper controllers are used to drive the deployers, each converting a direction and pulse input into stepper inputs. H-bridges are used to control the magnetorquers.

Table 1: Deployer Components

Letter	Component
A	Magnetorquer
B	AM1524 Stepper with 81:1 Gearbox
C	M3-0.5x50mm Socket Head Cap Screw (8x)
D	Sleeve
E	Female Shell Half
F	M2-0.4x4mm Flat Head Screw (3x)
G	Boom
H	Rollers (8x)
I	Drum, Bearings, and M3-0.5x4mm Flat Head Screws (4x)
J	Male Shell Half

When the spacecraft is initially deployed, the controller will first activate the B-dot magnetorquer de-tumble algorithm. When the spacecraft angular velocity is below a certain threshold, the controller will fully deploy the booms while running the B-dot de-tumble law to reduce oscillations in the attitude. Once the attitude has stabilized, the controller will stop running the B-dot law and will be ready to perform orbital maneuvering or targeted de-orbit algorithms by deploying and retracting the booms. The team is also considering using the space qualified Xiphos Q7 microcontroller for satellite missions where a higher degree of reliability is required. The Q7 has multiple copies of the operating system in different storage locations and implements active memory correction algorithms. It has been radiation tested and has significant space legacy [32].
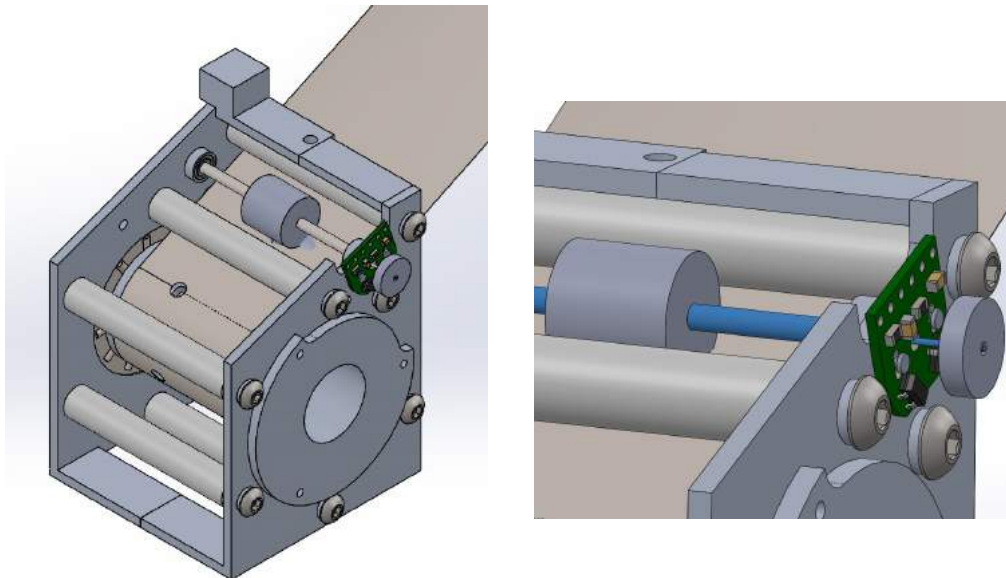
3.6. Future Improvements

Figure 8: Encoder Will Track Actual Motion of Boom

Control of a boom using the internal stepper motor causes the boom to intermittently wind up during the deploying and retracting processes and move in spurts in-

stead of extending/retracting continuously. This discontinuous motion results in uncertainty on the deployed length of the boom. A rotary encoder is currently being considered to measure the actual deployed length by tracking the rotation of one of the rollers. A urethane roller replaces one of the PTFE rollers and is used to turn the encoder wheel. The encoder will be used with an algorithm to control the motor and stop deployment or retraction at the appropriate point.

4. Environmental Forces and Torques

Gravitational, aerodynamic, and magnetic effects impart external forces and torques on the spacecraft. The modeling of these effects is discussed in this section.

4.1. Aerodynamic Drag

Aerodynamic drag force is given by the equation [33]

$$\vec{F_d} = -\frac{1}{2}C_d\rho A|\vec{v}_\infty|\vec{v}_\infty \tag{1}$$

where C_d is the drag coefficient, ρ is the density, A is a reference surface area, and $\vec{v}_\infty$ is the velocity vector of the spacecraft relative to the atmosphere. Because the atmosphere rotates at approximately the same rate of the Earth, $\vec{v}_\infty$ can be calculated by [34]

$$\vec{v}_\infty = \vec{v} - \vec{\omega}_e \times \vec{r} \tag{2}$$

where $\vec{v}$ is the orbital velocity and $\vec{r}$ is the position of the spacecraft, and $\vec{\omega}_e$ is the rotation rate of the Earth. Eqn. 1 can be divided by the spacecraft mass and re-written to calculate the acceleration due to drag

$$\vec{a_d} = -C_b\rho v_\infty \vec{v}_\infty \tag{3}$$

Where the ballistic coefficient C_b is given by

$$C_b = \frac{C_d A}{2m} \tag{4}$$

The greatest uncertainty in the drag force is associated with the drag coefficient and density, though models do exist for both. For completely specular reflection where particles do not interact with each other and where they reflect off the surface at the same angle at which they impact, the theoretical drag coefficient is two for a sphere and four for a flat plate perpendicular to the velocity vector if the area used for Eqn. 1 is the area of the plate or largest cross-section of the sphere [35]. The 1976 standard atmosphere [36] was used to calculate the density at various altitudes to characterize the behavior of the satellite under average orbital conditions. For a specific orbit, more advanced density models such as NRLMSISE-00 [37] can be utilized for increased accuracy.

To model the total aerodynamic drag force and torque, the spacecraft can be discretized into a collection of flat plates where the quaternion relating each plate to the spacecraft body frame is known. If specular reflection is assumed, for all plates where the angle between the surface normal vector and the velocity vector is greater than 90 degrees (surface is exposed to the air-stream), the component of the velocity vector perpendicular to the plate ($v_\perp$) can be calculated and used with Eqn. 1 to calculate the
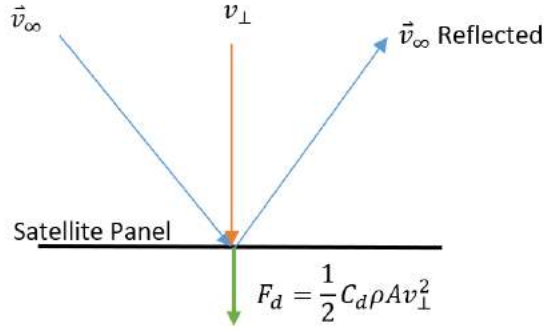
Figure 9: Calculating the Aerodynamic Drag Force on Each Satellite Panel

aerodynamic drag force acting at the geometric center of the plate as shown in Fig. 9. If $\vec{F}_{di}$ is the force acting on plate i and $\vec{r}_i$ is the vector from the satellite center of mass to the plate's geometric center, the total aerodynamic force ($\vec{F}_{dt}$) and torque ($\vec{T}_t$) acting on a satellite with n plates can be calculated by

$$\vec{F}_{dt} = \sum_{i=1}^{n} \vec{F}_{di} \tag{5}$$

$$\vec{T}_t = \sum_{i=1}^{n} r_i \times \vec{F}_{di} \tag{6}$$

Note that this method of aerodynamic modeling does not take into account the occlusion of some panels by other panels. Techniques have been developed to account for occlusion [38], but they were not implemented in this work because the geometry of the spacecraft was such that occlusion was not a significant factor in the total aerodynamic force and torque.

4.2. Gravitational Effects

The Earth's gravity is by far the dominant force acting on a spacecraft in low Earth orbit. The acceleration due to Earth's gravity including J_2 is given by Bate, Muller, and White [39]. Solar and lunar gravity do have an effect but that effect is negligible for LEO spacecraft and is not considered here.

There will always be some parts of a spacecraft that are closer to the Earth than others for any given attitude. The parts closer to Earth will experience a greater gravitational attraction resulting in a difference between the center of gravity and center of mass. This causes a gravity gradient torque which can be written in terms of the spacecraft principal moments of inertia and the spacecraft position vecto5r [40].

4.3. Magnetic Hysteresis Torques

Ferromagnetic components onboard a spacecraft spacecraft can easily become magnetized by the Earth's magnetic field. These components retain some of their magnetization as the spacecraft changes attitude and can interact with the Earth's magnetic field to produce a torque. This is known as magnetic hysteresis torque. Often, spacecraft with no active attitude control include hysteresis rods (long ferromagnetic rods) to reduce the spacecraft's rate of tumble. While properly sized hysteresis rods can reduce the steady state tumble rate, the hysteresis effect is not comparable

to that of a viscous damper. Hysteresis torques sometimes add angular momentum to the spacecraft and sometimes remove it. However, the amount of angular momentum removed, on average, tends to be more than the angular momentum added when above a certain angular velocity threshold. Below this threshold, the hysteresis torques will act as a disturbance and perturb the spacecraft's attitude. For systems such as this one with long booms, making these booms out of a ferromagnetic material could cause significant hysteresis torques which may result in undesired effects. While the fundamental physics behind magnetic hysteresis is not extremely well known, there are some mathematical techniques (based on experimental data) that can be utilized to characterize the hysteresis effects on a satellite and determine which materials to use.

The induced magnetic flux density in a metallic rod that has been exposed to some external sinusoidally varying magnetizing field is given by the hysteresis loop shown in Figure 10 which was taken from the NDT Resource Center [41]. When initially demagnetized and exposed to some external magnetizing field H (measured in Amps/meter), the magnetic flux density B (measured in Tesla) in the rod increases until it reaches its saturation value B_s (point a on the diagram). H must then be decreased to the coercivity point H_c (point c on the diagram) for B to become zero again. If H is reduced to zero, the rod will still retain some magnetic flux density value B_r (magnetic remanence) given by point b on the diagram. Reducing H beyond H_c decreases B until the saturation point $-B_c$ (point d). The cycle continues if H is increased again. The magnetic hysteresis properties of a material can be completely specified by H_c, H_r, and B_s. Note that when the term "magnetic field" is used, the B-field is what is often referred to although "magnetic field" has been traditionally reserved for H. As such, B will refer to the magnetic flux density and H will refer to the external magnetizing field for the purposes of hysteresis torque calculation. Magnetic field models such as the International Geomagnetic Reference Field (IGRF) [42] generally return the value of the B. B can be converted to H for use in hysteresis calculation by

$$B = \mu_0 H \tag{7}$$

where μ_0 is the permeability of free space.

Flatley and Henretty [43] found the *arctan* function to be a good fit to the hysteresis loop based on experimental data. The left boundary of the hysteresis loop can approximated by

$$B = \frac{2}{\pi} B_s \tan^{-1}\left[k(H + H_c)\right] \tag{8}$$

where B_s, B_r, and H_c are the saturation, remanence, and coercivity of the material in question and

$$k = \frac{1}{H_c} \tan\left(\frac{\pi B_r}{2 B_s}\right) \tag{9}$$

The right boundary of the hysteresis loop is similarly modeled by

$$B = \frac{2}{\pi} B_s \tan^{-1}\left[k(H - H_c)\right] \tag{10}$$

The slope of the boundary curve (either boundary) can be found by solving Eq. 8 for H, calculating the derivative with respect to H and then solving for dB/dH [43]. This

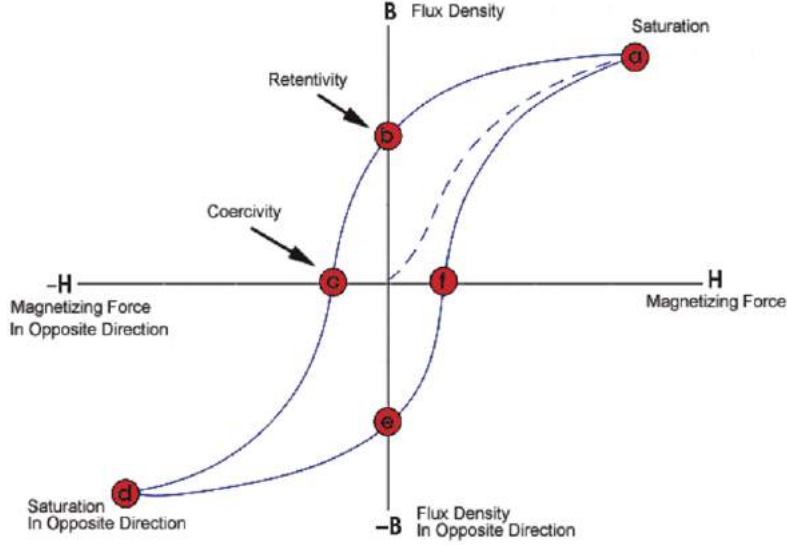**Figure 10: Magnetic Hysteresis Loop**

yields

$$B' = \left(\frac{dB}{dH}\right)_{bound} = \frac{2}{\pi} k B_s \cos^2\left(\frac{\pi B}{2 B_s}\right) \tag{11}$$

Note that this value of dB/dH is applicable only if the current value of B lies along the boundary of the hysteresis loop. There are many cases where B may not lie along this boundary such as when the simulation first starts with $B = 0$ and when the maximum value of H is not large enough to drive B all the way up to the saturation value of B_s. In this case, the actual value of dB/dH can be calculated based on the boundary slope (B') and the fractional distance from the corresponding boundary (f).

$$\frac{dB}{dH} = \left[q_0 + (1 - q_0)f^p\right] B' \tag{12}$$

where q_0 and p are empirically determined constants calculated to fit the experimental data and

$$f = \frac{|H - H_L|}{2 H_c} \tag{13}$$

If dH/dt is positive, the right boundary H_r is used in Eqn. 13, while if dH/dt is negative, the left boundary H_L is used in 13. With the ability to calculate dB/dH for any values of H and B, the time rate of change of the magnetic flux density induced in the boom can be calculated as

$$\frac{dB}{dt} = \frac{dB}{dH}\frac{dH}{dt} \tag{14}$$

dH/dt can be calculated by first determining the rate of change of H in the satellite body frame and taking the dot product of that vector with the vector along the boom axis. In addition to the attitude quaternion and ECI position and velocity vectors, the overall state vector in the simulation can be expanded to contain the magnitude of the magnetic flux density along each boom. The above procedure can be used to calculate dB/dt at each point in time. To simulate magnetic hysteresis, the state vector can be augmented to contain the current value of B for each boom during the numerical

13

integration. For each boom, the magnetic moment vector can be calculated as

$$\vec{\mu} = \frac{BV\vec{l}}{\mu_0} \tag{15}$$

where V is the volume of the boom, $\vec{l}$ is the vector along the length of the boom and μ_0 is the permeability of free space. The magnetic moments of all the booms can be summed and the total magnetic hysteresis torque can than be calculated by

$$\vec{T}_{hyst} = \vec{\mu}_0 \times \vec{B}_{Earth} \tag{16}$$

Where B_{Earth} is the magnetic field (flux density) of the Earth given directly by the IGRF model [42].

5. Active Attitude Control using Magnetorquers

When satellites are initially deployed, they generally experience some initial angular velocity and are in a "tumbling" state. To eliminate this initial angular velocity, external torques must be applied to the satellite. This can be accomplished using the popular B-dot de-tumble law [29] modified to ensure that the magnetorquer power draw is within acceptable limits.

5.1. B-Dot De-tumble Law

The magnetic moment vector generated by a magnetorquer is given by [44]

$$\vec{\mu} = IAn\hat{s} \tag{17}$$

where I is the current running through the magnetorquer, A is the area, n is the number of turns, and $\hat{s}$ is the unit vector normal to the coil measured in a right-handed sense such that the fingers of a right hand curl along the direction of the current if the thumb is pointing along $\hat{s}$. Assuming three orthogonal magnetorquers, a total magnetic moment vector can be created in any direction. Since magnetic torque involves a cross product of the magnetic field vector, the magnetic torque must be perpendicular to the magnetic field vector. Since magnetic torque is given by Eqn. 16, the set of possible commanded magnetic moments will be restricted to values of $\vec{\mu}$ perpendicular to $\vec{B}_E$ (the magnetic field of Earth) in order to maximize the resulting torque. Selecting the direction of $\vec{\mu}$ along the $^E\vec{\omega}^B \times \vec{B}_E$ vector where $^E\vec{\omega}^B$ is the angular velocity of the satellite body frame relative to the ECI frame ensures that the angle between the torque vector and the projection of $^E\vec{\omega}^B$ onto a plane perpendicular to $\vec{B}_E$ will be 180 degrees as shown in Fig. 11. For a given magnitude of $\vec{\mu}$, this direction generates a torque vector that will serve to reduce the overall spacecraft angular momentum more than would the torque vector generated by placing $\vec{\mu}$ along any other direction. The total magnetic moment vector associated with the B-dot law can be calculated as:

$$\vec{\mu}_{tot} = -k\dot{\vec{B}}_E \tag{18}$$

where k is a constant gain selected based on the strength of the magnetorquers and the desired performance and $^B\dot{\vec{B}}_E$ is the time rate of change of the magnetic field vector as observed in the satellite body frame given by
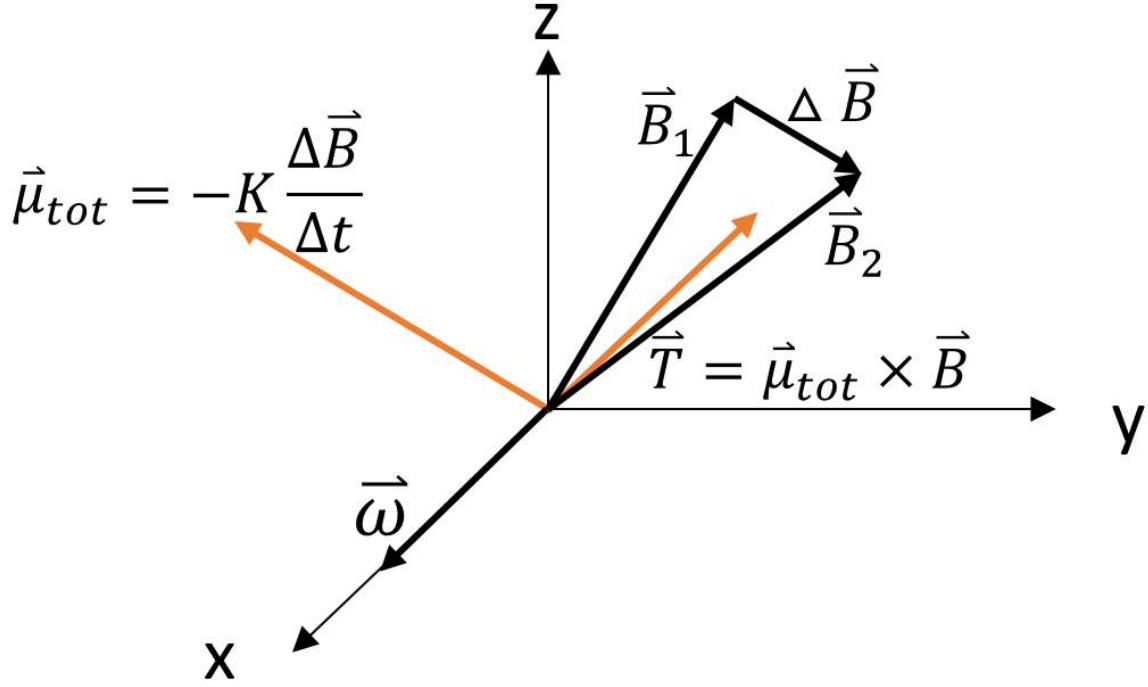
Figure 11: Magnetic Moment and Torque from B-Dot Detumble Law [45]

$$^B\dot{\vec{B}}_E = \frac{^B d\vec{B}_E}{dt} = \vec{B}_E \times {^E\vec{\omega}^B} = \frac{\vec{B}_{E2} - \vec{B}_{E1}}{\Delta t} \tag{19}$$

In some implementations, the unit vector in the $^B\dot{\vec{B}}$ direction is used in Eqn. 18, but the system will remain stable and effectively de-tumble the satellite either way. If the power P_{req} required to achieve the initially desired $\vec{\mu}_{tot_0}$ from Eq. 18 is greater than the maximum power P_{max} allocated to the B-dot law, $\vec{\mu}_{tot}$ can be reduced in magnitude to ensure that the required power is equal to P_{max} by performing the operation

$$\vec{\mu}_{tot} = \vec{\mu}_{tot_0} \sqrt{\frac{P_{max}}{P_{req}}} \tag{20}$$

Once the current required for each magnetorquer is calculated using Eqn. 17, the power required to achieve the current is given by

$$P_{req} = I^2 R \tag{21}$$

where R is the electrical resistance of the magnetorquer coil.

Unlike magnetic hysteresis torques, active magnetic control using B-dot does act similarly to a velocity damper and can reduce the total spacecraft angular velocity to a very low final value (around 2 rotations per orbit in practice).

An aerodynamic or gravity gradient stabilized satellite with no active damping will oscillate like an undamped pendulum about the equilibrium point. In addition to de-tumbling the satellite, the B-dot law can also be employed as a velocity damper to reduce the amplitude of these oscillations and minimize the steady state pointing error. The B-dot law can be de-activated once the satellite reaches its steady state pointing behavior.

6. Design Analysis and Simulations

Two goals of D3 are to facilitate the de-orbit of a 12U spacecraft from 700 km in 25 years and to provide a ram-aligned spacecraft attitude in order maximize the surface area perpendicular to the velocity vector and provide a predictable drag profile. The D3 also required the ability to deploy and retract in order to perform orbital maneuvers through variations in the aerodynamic drag force. Using the aforementioned modeling techniques, simulations were conducted to determine the drag device surface area required to meet the 25 year de-orbit time requirement and to assess the ability of the drag device to maintain the spacecraft in a ram-aligned attitude. The theory and analysis behind these simulations are discussed here. A method of partially deploying some of the booms to achieve 3-axis attitude stabilization using aerodynamic and gravity gradient forces was also investigated via simulations.

6.1. Orbit Lifetime Analysis

The orbit lifetime of a spacecraft in LEO is directly related to the amount of aerodynamic drag the spacecraft experiences. If a spacecraft with some ballistic coefficient C_{b1} (as defined in Eqn. 4) requires some amount of time Δt_1 to de-orbit, the de-orbit time Δt_2 for another spacecraft with the same initial conditions but a different ballistic coefficient can be estimated by

$$\Delta t_2 = \frac{C_{b1}\Delta t_1}{C_{b2}} \tag{22}$$

Eqn. 22 is very powerful because it allows the orbit lifetime for various satellite configurations to be estimated after conducting a single orbital simulation. Eqn. 22 is proven in this author's previous work for circular orbits where density is a function of semi major axis [22].

To approximate the orbit lifetime for various initial circular orbit altitudes, a single trajectory was propagated until de-orbit from an 800 km orbit with $C_{b_{sim}} = .1333\frac{m^2}{kg}$ assuming a spherical Earth and 1976 standard atmosphere for density calculations. In reality, the Earth is not a perfect sphere and the density at each altitude is not fixed, but these assumptions provide a good benchmark for high level analysis. After propagation was complete, Eqn. 22 was utilized to estimate the orbit lifetimes for satellites with different ballistic coefficients. Starting the simulation from 800 km provided the orbit lifetime for all initial circular orbit altitudes at and below 800 km.

To calculate the area of a drag device needed to de-orbit a 12U (15 kg) spacecraft from 700 km in 25 years, Eqn. 22 was first utilized to calculate the C_b needed to de-orbit from an altitude of 700 km. Given the simulated orbit lifetime of a spacecraft initially in a 700 km altitude circular orbit with $C_{b_{sim}}$, the required C_b value was

$$C_{b_{req}} = \frac{C_{b_{sim}}\Delta t_{sim}}{25\ years} = \frac{(.1333)(6.25)}{25} = .0333 \tag{23}$$

The drag coefficient of a spacecraft in free molecular flow with completely specular reflection will range from 2 for a sphere to 4 for a flat plate [35]. Assuming a drag coefficient of two as a conservative estimate, the surface area of the drag device needed to achieve a C_b of .0333 for a 15 kg spacecraft can be calculated from Eqn. 4 as

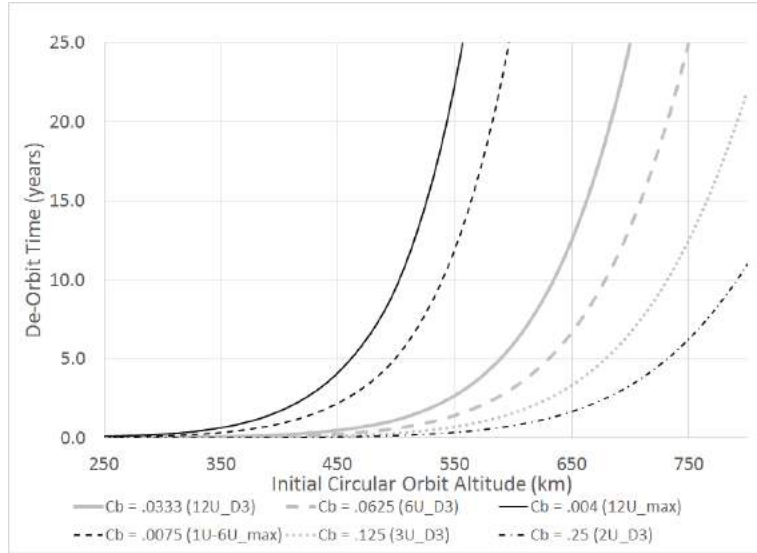$$A_{req} = \frac{2C_b m}{C_d} = \frac{2(.0333)(15)}{2} = .5m^2 \tag{24}$$

16

Figure 12: Orbit Lifetime vs. Initial Circular Orbit Altitude

To better illustrate the expected performance of the D3 on a variety of platforms, Figure 12 displays the orbit lifetime vs. initial altitude for spacecraft with ballistic coefficients corresponding to various geometries with and without the drag device. Included are orbit lifetimes for 12U, 6U, 3U, and 2U satellites weighing 15, 8, 4, and 2 kg respectively and equipped with the drag device (area of $.5m^2$). Also included are orbits lifetimes for 12U and 1U-6U spacecraft with no deployables oriented with their largest faces perpendicular to velocity. Note that the drag coefficient of all spacecraft was assumed to be two as a conservative estimate. Overall, the D3 significantly reduces the orbit lifetime of nearly any legacy CubeSat configuration.

6.2. Attitude Dynamics Simulations and Results

Simulation results demonstrated that the D3 design detailed in Section 3 provided aerodynamic stability up to an altitude of 700 km. These results also showed that making the boom angle less than 20 degrees significantly reduced attitude stability without appreciably increasing the surface area, while for angles greater than 20 degrees, the decrease in surface area was not justified by the slight increase in stability. Additionally, some of the booms could be partially deployed or retracted to create a clear spacecraft minimum moment of inertia axis that would align with the nadir vector due to gravity gradient torques. The non-magnetic Austenitic 316 stainless steel was selected as the material for the booms because hysteresis effects were deemed to be excessively large with ferromagnetic booms. The drag device will also contain a magnetometer and five magnetorquers in order to de-tumble the spacecraft and damp attitude oscillations using the B-dot de-tumble controller. Discussed below are the results of the various simulations that substantiated these decisions.

Note that in all simulations, the attitude of the spacecraft body frame (Fig. 1) is specified with respect to the orbital frame. The orbital frame is defined as shown in Fig. 13 with its origin on the satellite center of mass such that the z points toward the Earth, the y-axis is opposite the orbit angular momentum vector, and the x-axis completes the right handed coordinate system, where $x = y \times z$. In a circular orbit, the x-axis is aligned with the orbit velocity vector.
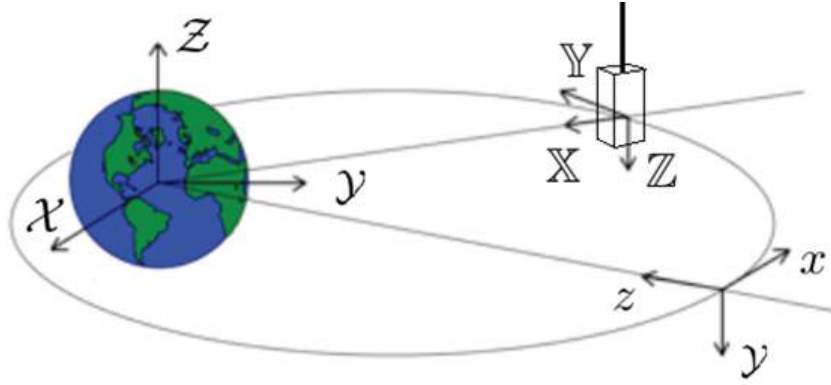
17

Figure 13: Schematic of ECI, Orbital, and Body Frames

6.2.1. Detumble Phase

The first simulation characterized the spacecraft's behavior immediately after deployment from the launch vehicle and included only magnetic torque due to the B-dot de-tumble controller. The satellite was assumed to have an initial tumble rate of 5 rotations per minute with the booms retracted. The IGRF magnetic field model of the Earth [42] was used and provided the value of the magnetic field at each time step based on the spacecraft position. Using B-dot alone, it was possible to get an angular velocity under .02 rpm within 12 hours. In practice, B-dot would remain active until the spacecraft is below a certain angular velocity threshold before deploying the booms. Figures 14 and 15 illustrate the satellite angular velocity over time when running B-dot and the magnetorquer power consumption. The pointing error is defined as the angle between the satellite z-axis (see Figure 1) and the velocity vector. This error oscillates without stabilizing because there are no aerodynamic torques to align the satellite with the velocity vector. Note that the magnetorquer power consumption after the initial de-tumble is almost zero.

6.2.2. Simulating Aerodynamic Stabilization

The next simulation included magnetic torque from the B-dot algorithm, aerodynamic torques corresponding to all booms fully deployed, and gravity gradient torques corresponding to all booms fully deployed. The simulation shown in Figure 16 illustrates the expected system performance and stability with non-ferromagnetic booms. With the booms fully deployed, the z-axis of the satellite is the maximum moment of inertia axis. Because gravity gradient torques work to align the minimum moment of inertia axis with the nadir vector, the maximum moment of inertia axis must be perpendicular to the nadir vector; a constraint which helps maintain ram-alignment.

6.2.3. Simulating Magnetic Hysteresis

The system from Section 6.2.2 was simulated with the inclusion of hysteresis torques due to the potential magnetization of the booms. Fig. 17 demonstrates the hysteresis effects on booms made of wrought iron (one of the most ferromagnetic materials). As shown, the hysteresis torques dominate the aerodynamic and gravity gradient torques and result in system instability. This behavior is consistent with conclusions reached
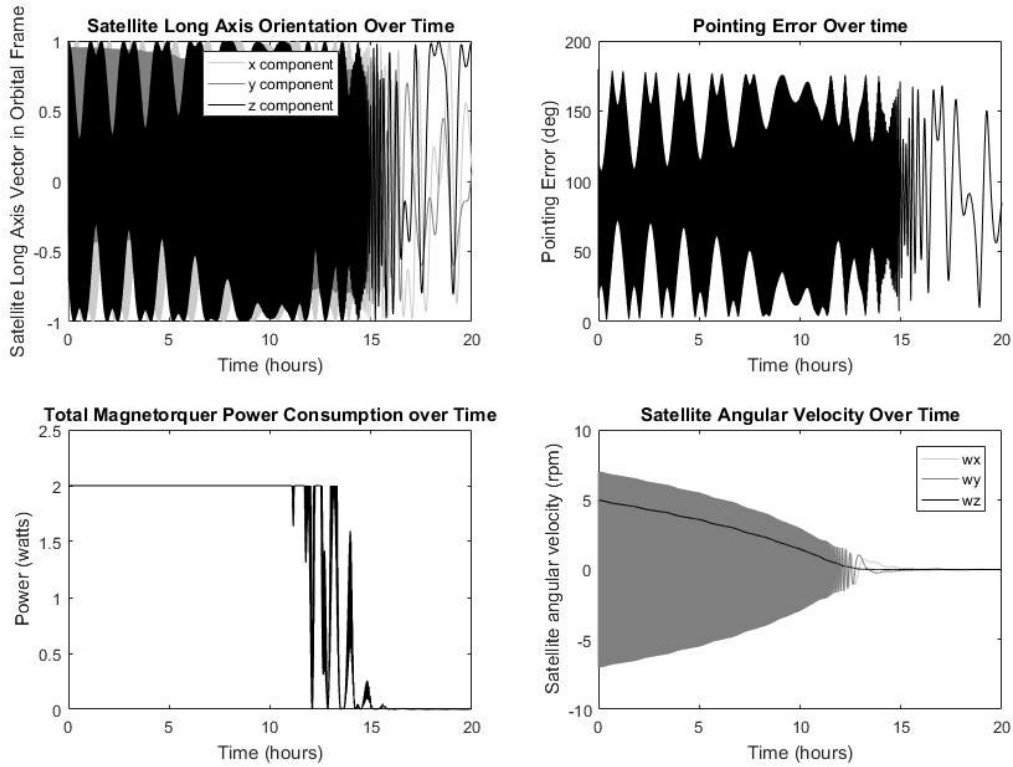
18

Figure 14: B-Dot Only in 700 km Circular Orbit

by other researchers through analyses and flight demonstrations that while hysteresis torques can help reduce the initial rate of tumble, they act as disturbances in the steady state [46, 47]. For this reason, the idea of using ferromagnetic booms such as pre-manufactured steel measuring tapes was abandoned and Austenitic 316 stainless steel was decided upon due to its ductility, low melting point compared to other alloys of stainless steel, and low ferromagnetism.

6.2.4. Three Axis Stabilization using Aerodynamic and Gravity and Gradient Torques

An added benefit of having retractable booms is the ability to align one axis of the satellite with the nadir vector using gravity gradient torques. By having two booms that are opposite each other partially deployed and having the remaining two booms fully deployed, the spacecraft minimum moment of inertia axis will be aligned with the two fully deployed booms and will align with the nadir vector. With aerodynamic torques constraining the z-axis of the satellite to align with the velocity vector, the spacecraft will be 3-axis stabilized. This ability is useful if an antenna or science instrument needs to point toward the ground (nadir), away from the ground (zenith), or toward the velocity vector. Fig. 18 shows the attitude dynamics when two of the booms are deployed half-way and the other two are fully deployed. Note that the graphs provide the components of each satellite body axis expressed in the orbital frame. Despite the reduction in aerodynamic torque, the spacecraft z-axis aligns with the velocity vector and the axis along the two fully deployed booms (x-axis in this case) aligns with the nadir vector.

A drawback of gravity gradient stabilization is that configurations with the minimum moment of inertia axis aligned with either the nadir or zenith vector will be stable.
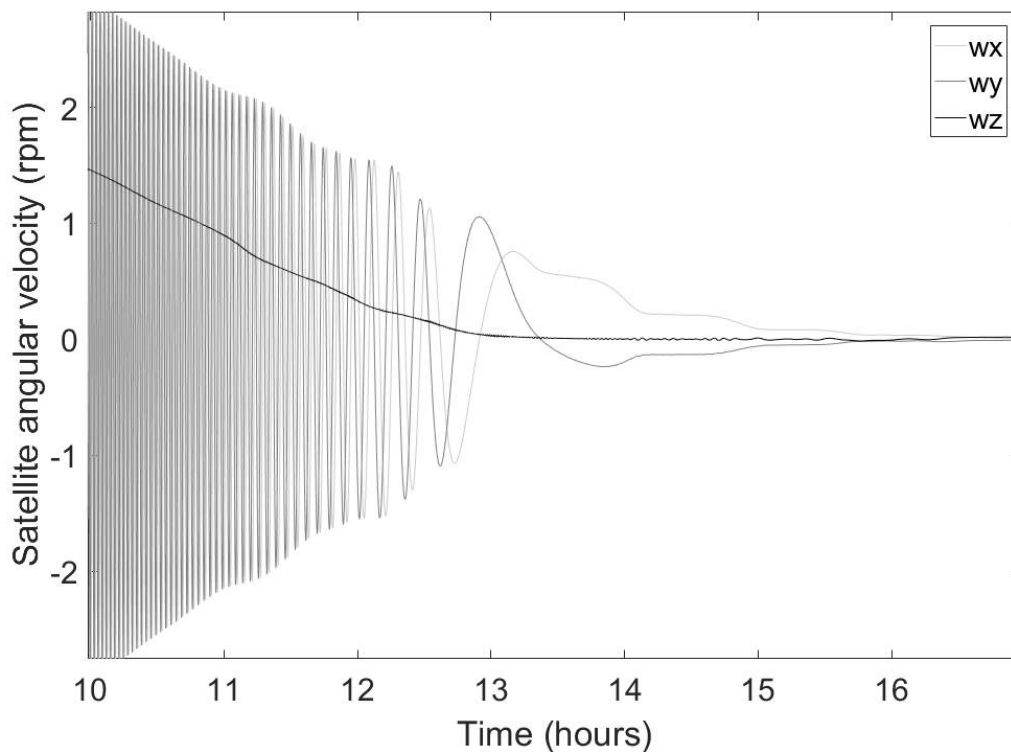
19

Figure 15: Angular Velocity when Simulating B-Dot Torques Only in 700 km circular orbit

However, if the satellite stabilizes in the wrong orientation, it may be possible to roll the satellite by asymmetrically deploying the booms so that the minimum moment of inertia axis lies 45 degrees offset from its original value. After waiting for the attitude to stabilize, another 45 degree rotation can be performed. The process can be continued until the spacecraft has been rotated 180 degrees to align the minimum moment of inertia axis with the nadir or zenith vector as desired. Alternatively, if it is desired to align the y-axis with the nadir vector, the booms along the x-axis can first be fully deployed and the y-axis booms partially deployed such that the x-axis has minimum moment of inertia and aligns with the nadir/zenith vector. In that case, only two 45 degree rotations will be needed to align the y-axis with the nadir vector. The control logic by which the booms are deployed and retracted to properly align the satellite will be investigated in future work.

7. Thermal Simulations

After completion of the preliminary design, two Thermal Desktop ® simulations were used to determine the system's thermal profile. Different outer thermal coatings for the system components were considered to ensure an acceptable temperature range. A 500 km altitude, 89 degree, sun synchronous orbit was used for the maximum heating case. A 500 km equatorial orbit was used as the case with maximum thermal cycling, due to the large changes in solar heating as the satellite moves in and out of eclipse.

Some simplifications were used for the thermal model. Heat transfer between the D3 outer structures and the environment, and conduction through the D3 major struc-
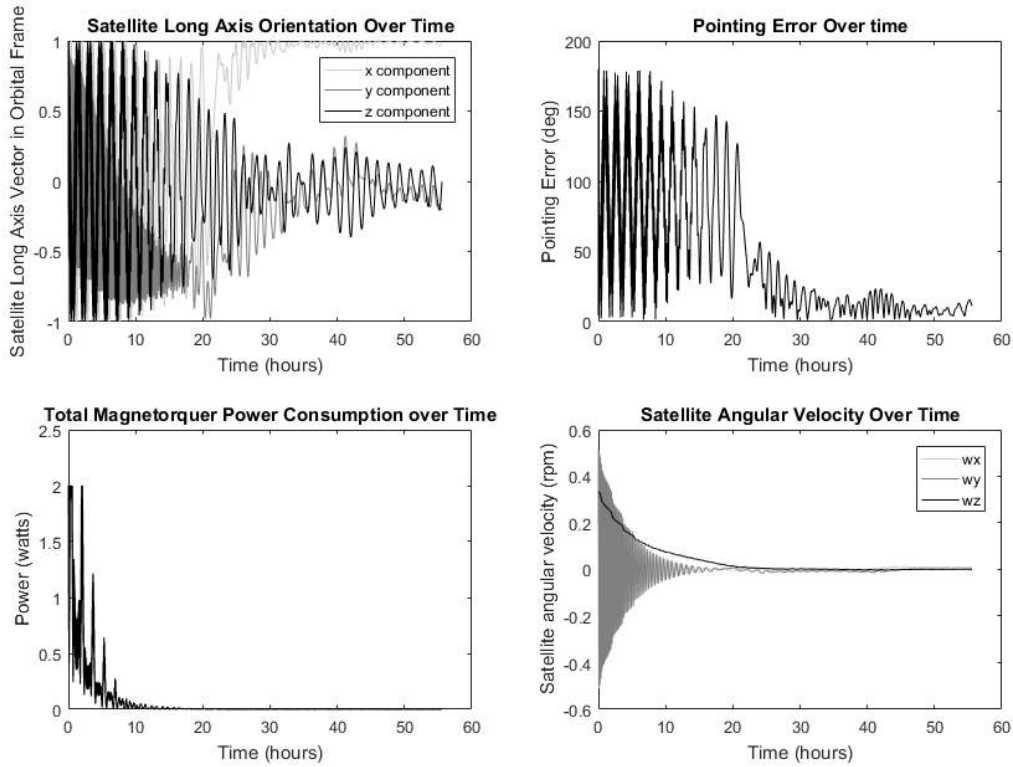
20

Figure 16: Aerodynamics, Gravity Gradient, and B-Dot torques for Fully Deployed Drag Device in a 700 km Circular Orbit

tures have both been considered. Table 2 shows the materials and surface treatments for the major parts of the system.

Table 2: D3 Materials and Optical Properties

Structure	Material	Surface Treatment	Solar Absorptivity	IR Emissivity
Shell	6061 Aluminum	None	0.44	0.143
Base	6061 Aluminum	None	0.44	0.143
Booms	316 Stainless Steel	None	0.39	0.11

The temperatures of the booms and shells for both sample orbits are shown in Fig. 19. As expected, the sun-synchronous orbit showed a nearly constant temperature for both components, since the heat flux was nearly constant. In comparison, the equatorial orbit showed significant temperature fluctuations, especially for the booms, as the satellite passed into and out of eclipse.

Since the D3 system and accompanying spacecraft will have several computer boards, internal temperatures must be kept within the operating ranges of these boards. The component temperatures shown in Fig. 19 would most likely result in the computer boards exceeding their operational limits and failing.

One solution to reduce the average temperatures is to anodize the aluminum components of the system, and combine sandblasting and passivation for the booms. The properties of these coatings are summarized in Table 3. Anodizing is an electrochemical process which can increase the emissivity of a material, leading to increased heat
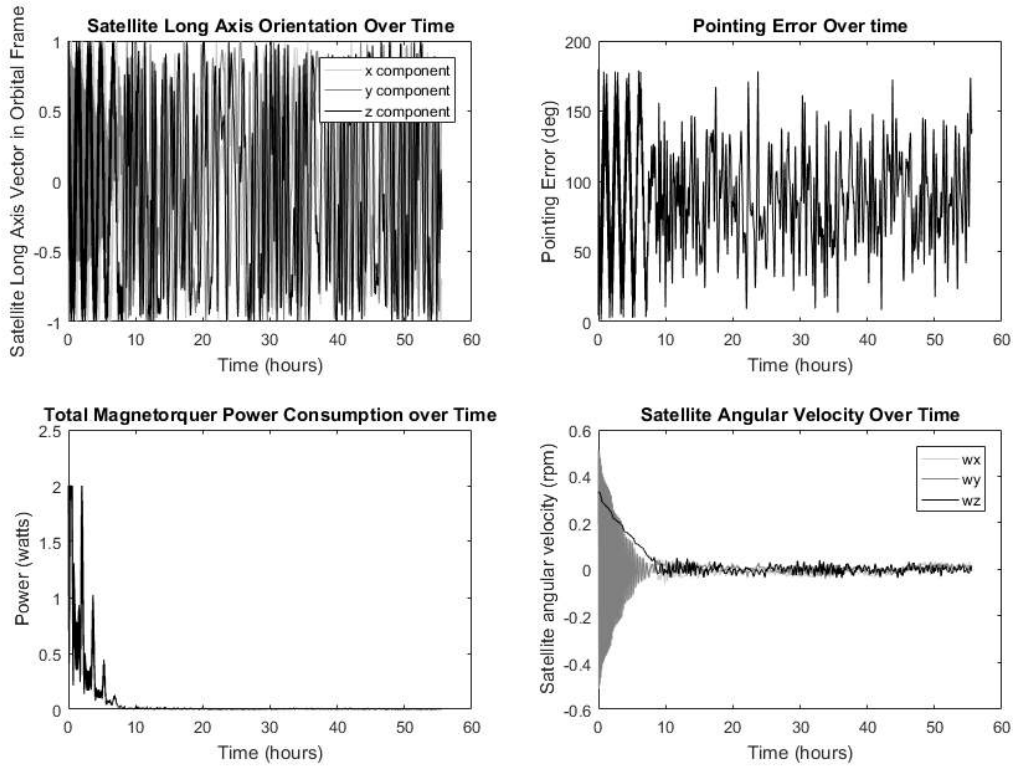
Figure 17: Aerodynamics, Gravity Gradient, B-Dot, and Hysteresis Torques for Fully Deployed Drag Device in a 700 km Circular Orbit

loss through radiation and a lower equilibrium temperature. Sandblasting involves sending a stream of abrasive particles at the stock, making the surface rougher. This will increase emissivity, at the cost of also increasing the absorptivity. To combat this, passivation is used. Passivation uses acid to remove surface contaiminants and oxidation. A new oxidation layer is formed afterward, reducing both absorptivity and emissivity. Fig. 20 shows the resulting temperature profile after the surface treatments.

Table 3: D3 Materials and Optical Properties After Surface Treatment

Structure	Material	Surface Treatment	Solar Absorptivity	IR Emissivity
Shell	6061 Aluminum	Anodized	0.44	0.56
Base	6061 Aluminum	Anodized	0.44	0.56
Booms	316 Stainless Steel	Sandblasting and passivation	0.38	0.38

7.1. Thermal Conclusions and Considerations

Anodizing the aluminum shells and sandblasting and passivating the booms results in boom temperatures between about -94 and 68 degrees C and shell temperatures between 0 and 80 degrees C depending on the orbit. This range is acceptable for the D3 components. The board containing the onboard computer and magnetorquer and motor driver chips will be thermally isolated from the outer structure to prevent excessive thermal cycling.
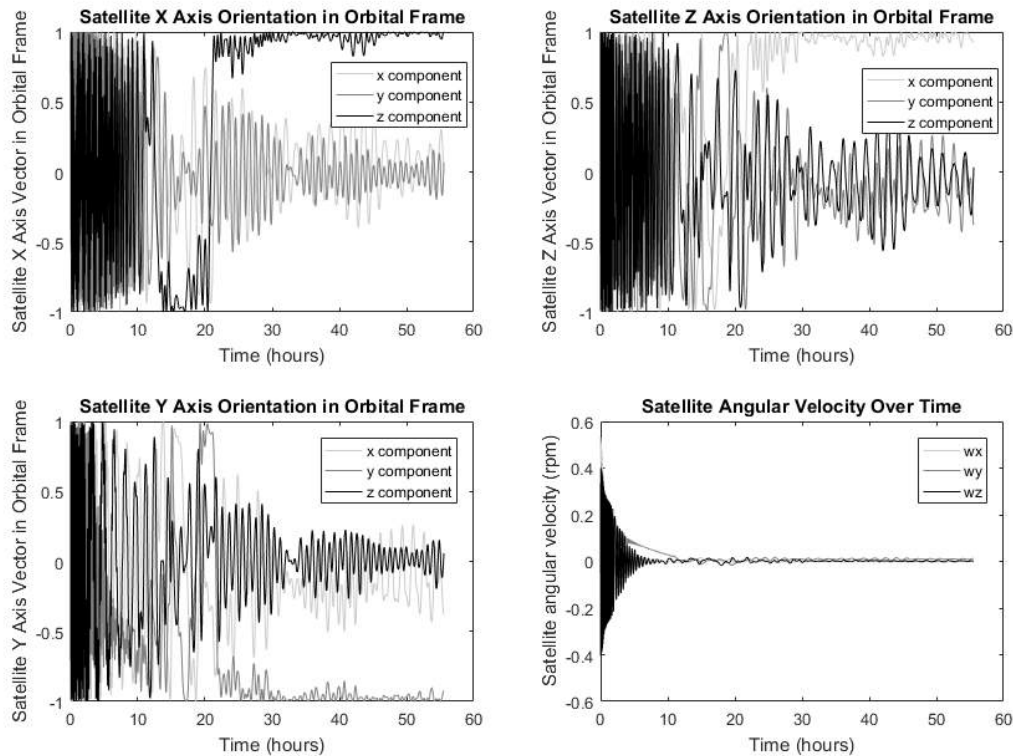
22

Figure 18: 3-axis Attitude Stabilization using Gravity Gradient and Aerodynamic Torques in 700 km Circular Orbit

Additionally, the device is intended to burn up on re-entry such that no additional debris is created. The D3 components with the highest melting points are the booms made of Austenitic 316 steel which will melt at around 1380 degrees C. Utilizing a re-entry thermal analysis tool developed by the NASA Kennedy Space Center, it was determined that the booms and all other D3 components would disintegrate completely upon re-entry even if the booms were fully coiled.

8. Deployer Testing

8.1. Repeated Cycling of Motor

To ensure the deployer would repeatedly actuate in the course of the mission, both repetition and vacuum testing were performed. The deployer was successfully cycled through its full length for 500 repetitions. Since the equivalent of only a few dozen full cycles will be required in orbit, this was deemed more than sufficient. The only issue encountered while deployment testing involved the screws loosening. In practice, this will not be an issue since the screws will be held in place with epoxy while in orbit.

The deployment cycling primarily wears down the inside of the shells as shown in Fig. 22. This is due to the hard steel boom wearing the comparatively softer aluminum inner shell away. The boom tends to touch the sides of the shell during deployment, but as the sides wear away, this becomes less of a problem. The wear on the shell was not large enough to cause any structural issues after 500 cycles.

Other wear locations can be found by searching for aluminum particles. Particles were also found in the bearings and on the inside and outside of the drum. Some wear
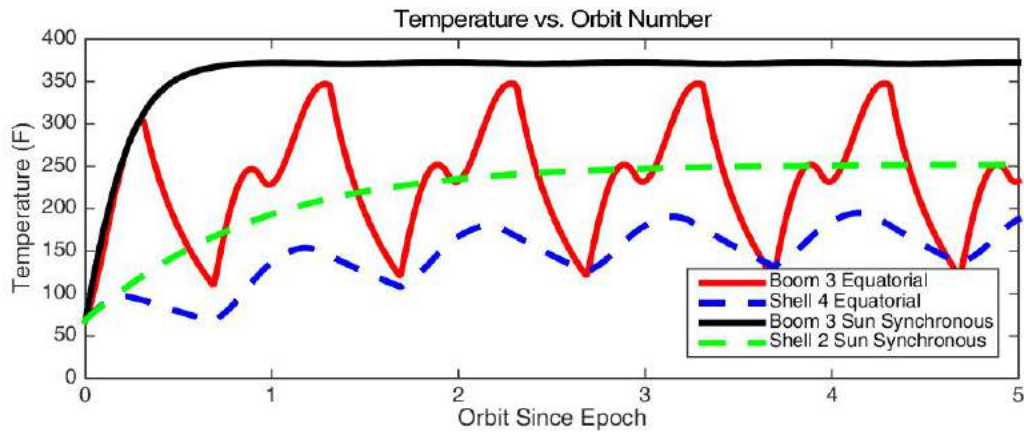
23

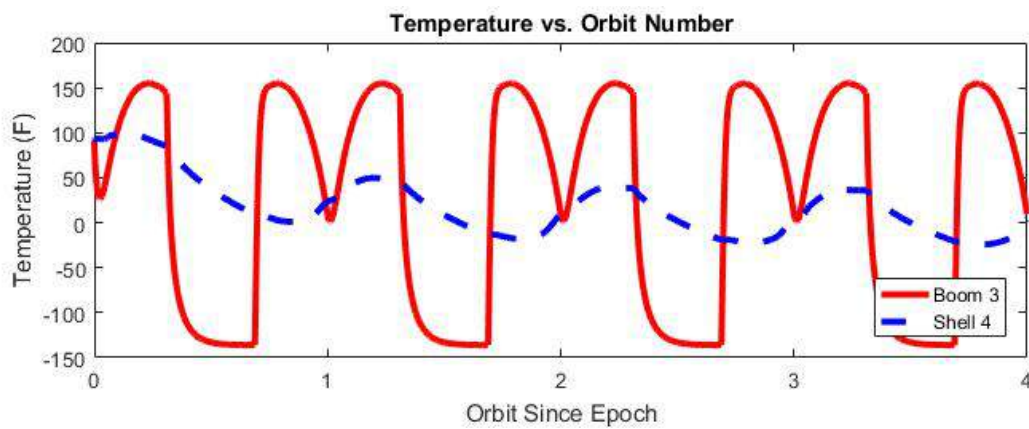**Figure 19: On-Orbit Temperatures Estimated via Numerical Simulations**

Figure 20: Approximate Temperatures in Equatorial Orbit, After Surface Treatment

particles were also found embedded in the rollers, but these were likely carried by the boom, since there is no sliding contact between the boom and rollers. More detailed views can be found in Fig. 23.

8.2. Thermal Vacuum Testing

Since the deployers are designed to work in LEO, a deployer was operated at different temperatures in a vacuum chamber. Two thermocouples were used to track the temperature. The first was placed on the motor to keep it from overheating, and the second was on the shell by the gearbox output, opposite the motor. These represented the expected hottest and coolest components, respectively. The location of both thermocouples can be seen in Fig. 24.
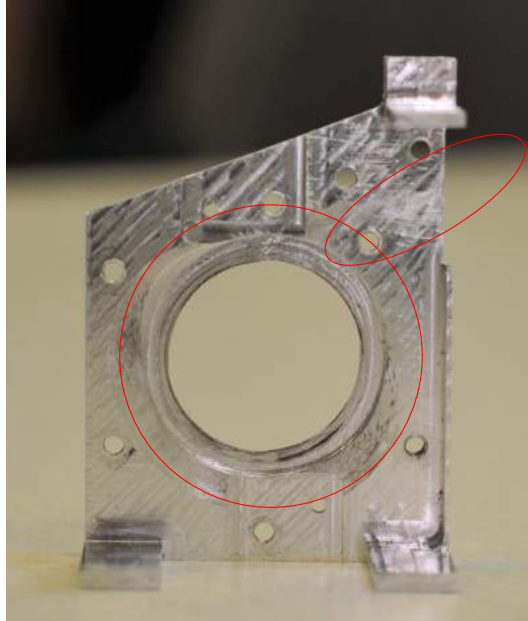

Figure 21: Deployer Extended Along Table

24

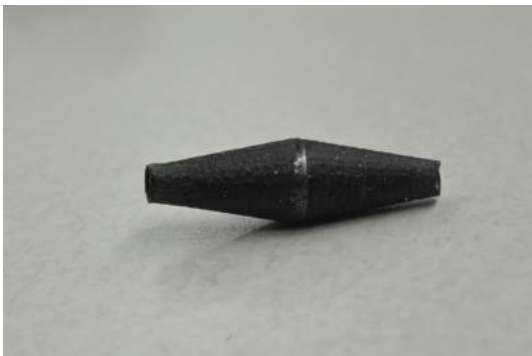**Figure 22: Inner Shell Wear (Worn Areas Circled)**

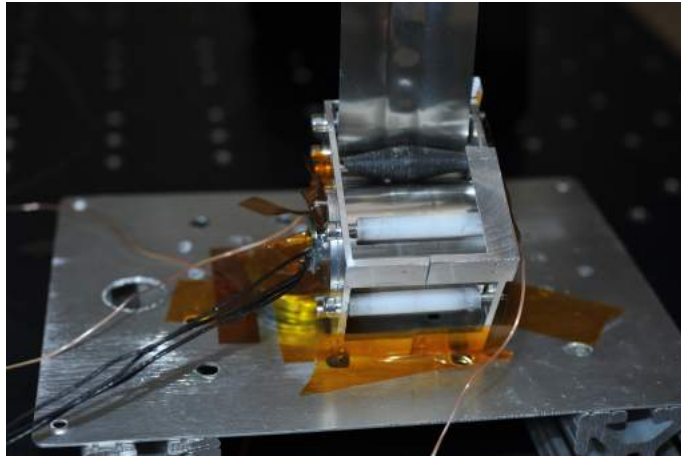**Figure 23: Aluminum Particles Show Wear Locations**
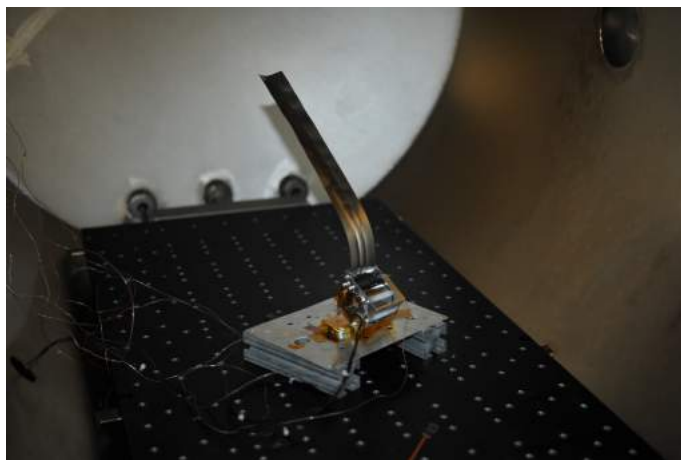
Figure 24: Thermocouple Locations

Figure 25: Boom Curved Unexpectedly in Thermal Vacuum Chamber

Using the shell thermocouple as the reference point, the shell temperature was cycled to match the NASA LSP qualification test as closely as possible [48]. The shell temperature was first dropped to -5C at a pressure of $2 * 10^{-6}\ Torr$, the lower limit of the chamber. The deployer then underwent 20 shortened deploy/retract cycles due to test chamber size limitations, or the equivalent of approximately 5 full cycles. Next, the temperature was raised to 55C at a pressure of $6 * 10^{-5}\ Torr$, and the deployer was again taken through 20 shortened cycles.

The motor used was not vacuum rated but has been used in vacuum testing of previous iterations of the deployer. Both the high and low temperature cycles worked without issue. The motor experienced significant temperature rise during both cycles, rising from -1 C to 70 C, then 49 C to 86 C. This is within the allowable temperature range of the motor [31] and represents several continuous cycles, which would not happen in orbit.

The boom experienced some unexpected curvature while in the thermal vacuum chamber, curving opposite the expected direction (shown in Fig. 25). This was found to be a result of the previous testing having run along the table, putting a backwards curve in the boom. Prior repeated cycling with the deployer suspended from the ceiling and the boom oriented downwards to prevent backwards bending did not produce any permanent deformation.

9. Conclusions

The goal of the Drag De-Orbit Device (D3) is to enable a 12U (15 kg) CubeSat to de-orbit in 25 years from a 700 km circular orbit while providing passive attitude stability and a means of modulating the drag area for orbital maneuvering purposes. To achieve this, the D3 is designed with four retractable tape-spring booms, each 4 cm wide (when flat), 3.7 m long, and inclined at 20 degrees relative to the top face of the satellite for a total drag area of $.5m^2$. It was shown through simulations that a system in this configuration would be aerodynamically stable up to an altitude of 700 km and would align the z-axis of the satellite (Figure 1) with the velocity vector, providing a predictable attitude profile and maximizing aerodynamic drag. The booms of the drag device could also be differentially deployed such that the resulting gravity gradient torques align a satellite axis perpendicular to the z-axis with the nadir vector. The ability to modulate the spacecraft's drag area by deploying and retracting the booms means that this device could be used for orbital maneuvering, collision avoidance, and the targeting of a re-entry point using only aerodynamic forces. Thermal analysis showed that a proper surface finish applied to the booms and boom deployer shells would ensure that all D3 components operate within their thermal limits. Additional thermal analysis also showed that the entire system would disintegrate on re-entry and would not create any additional debris. Fatigue testing and thermal vacuum testing verified the ability of the D3 to function in the space environment.

D3 is the first spacecraft subsystem capable of providing passive 3-axis attitude stabilization while simultaneously modulating the drag area of the host spacecraft. On many missions, use of the D3 would eliminate the need for large, expensive, complex legacy attitude control and thruster systems. After the planned flight demonstration, the D3 has the potential to become a standard tool in orbit and attitude control and debris mitigation for small satellites.

Acknowledgments

References

[1] J. C. Liou, Collision Activities in the Future Orbital Debris Environment, Advances in Space Research 38 (2006) 2102–2106. http://dx.doi.org/10.1016/j.asr.2005.06.021.

[2] H. Heidt, J. Puig-Suari, A. Moore, S. Nakasuka, R. Twiggs, CubeSat: A New Generation of Picosatellite for Education and Industry Low-Cost Space Experimentation, in: Proceedings of the 14th Annual AIAA/USU Conference on Small Satellites, Logan, UT. http://digitalcommons.usu.edu/smallsat/2000/All2000/32.

[3] A. Marinan, A. Nicholas, K. Cahoy, Ad-hoc CubeSat Constellations: Secondary Launch Coverage and Distribution, in: 2013 IEEE Aerospace Conference. http://dx.doi.org/10.1109/AERO.2013.6497174.

[4] Nasa Technical Standard NASA-STD-8719.14A, 2011. https://standards.nasa.gov/file/2639/download?token=vq9sWsAS.

[5] The Kessler Syndrome: Implications to Future Space Operations, Univelt, Inc., ???? Proceedings of the 33rd Annual AAS Guidance and Control Conference.

[6] R. P. Hoyt, I. M. Barnes, N. R. Voronka, J. T. Slostad, The Terminator Tape: A Cost-Effective De-Orbit Module for End-of-Life Disposal of LEO Satellites, in: Proceedings of the AIAA Space 2009 Conference.

[7] R. L. Forward, R. P. Hoyt, C. W. Uphoff, Terminator Tether™: A Spacecraft Deorbit Device, Journal of Spacecraft and Rockets 37 (2000) 187–196. http://dx.doi.org/10.2514/2.3565.

[8] J. Andrews, K. Watry, K. Brown, Nanosat Deorbit and Recovery System to Enable New Missions, in: Proceedings of the 2011 SmallSat Conference.

[9] K. T. Nock, K. L. Gates, K. M. Aaron, A. D. McRonald, Gossamer Orbit Lowering Device (GOLD) for Safe and Efficient De-Orbit, in: Proceedings of the 2010 AIAA/AAS Astrodynamic Specialist Conference.

[10] P. Harkness, M. McRobb, P. Lützkendorf, R. Milligan, A. Feeney, C. Clark, Development Status of AEOLDOS - A Deorbit Module for Small Satellites, Advances in Space Research 54 (2014) 82–91. https://doi.org/10.1016/j.asr.2014.03.022.

[11] D. C. Maessen, E. D. van Breukelen, B. T. C. Zandbergen, O. K. Bergsma, Development of a Generic Inflatable De-Orbit Device for CubeSats, in: Proceedings of the 58th International Astronautical Congress.

[12] D. Reintsema, J. Thaeter, A. Rathke, W. Naumann, P. Rank, J. Sommer, DEOS-the German Robotics Approach to Secure and De-Orbit Malfunctioned Satellites from Low Earth Orbits, in: Proceedings of i-SAIRAS 2016, pp. 244–251.

[13] P. C. E Roberts, P. G. Harkness, Drag Sail for End-of-Life Disposal from Low Earth Orbit, Journal of Spacecraft and Rockets 44 (2007) 1195–1203. https://doi.org/10.2514/1.28626.

[14] B. Cotton, On-Orbit Results from CanX-7 Drag Sail De-Orbit Mission, in: Proceedings of the 31st Annual AIAA/USU Conference on Small Satellites, Logan, Utah. http://digitalcommons.usu.edu/cgi/viewcontent.cgi?article=3672&context=smallsat.

[15] R. P. Patera, K. R. Bohman, M. A. Landa, C. Pao, R. T. Urbano, M. A. Weaver, D. C. White, Controlled Deorbit of the Delta IV Upper Stage for the DMSP-17 Mission, in: Proceedings of the 2nd IAASS Conference Space Safety in a Global World.

[16] V. Luchinski, R. Murtazin, O. Sytin, Y. Ulybyshev, Mission Profile of Targeted Splashdown for Space Station Mir, Journal of Spacecraft and Rockets 40 (2003) 665–671. http://arc.aiaa.org/doi/abs/10.2514/2.6915.

[17] R. P. Patera, W. H. Ailor, The Realities of Reentry Disposal, in: Proceedings of the 1998 AAS/AIAA Space Flight Mechanics Meeting, pp. 9–11.

[18] C. L. Leonard, Formationkeeping of Spacecraft via Differential Drag, Master's thesis, Massachusetts Institute of Technology, 1986.

[19] T. D. Maclay, C. Tuttle, Satellite Station-Keeping of the ORBCOMM Constellation Via Active Control of Atmospheric Drag: Operations, Constraints, and Performance, Advances in the Astronautical Sciences 120 (2005) 763–773.

[20] B. Kumar, A. Ng, Japan Canada Joint Collaboration Satellite - Formation Flying (JC2Sat-FF) Mission Design, 2013. Case Study.

[21] D. Pérez, R. Bevilacqua, Differential Drag-Based Reference Trajectories for Spacecraft Relative Maneuvering Using Density Forecast, Journal of Spacecraft and Rockets 53 (2016 http://dx.doi.org/10.2514/1.a33332) 234–239.

[22] S. R. Omar, R. Bevilacqua, D. Guglielmo, L. Fineberg, J. Treptow, S. Clark, Y. Johnson, Spacecraft Deorbit Point Targeting Using Aerodynamic Drag, Journal of Guidance, Control, and Dynamics 40 (2017) 2646–2652. https://arc.aiaa.org/doi/10.2514/1.G002612.

[23] R. Bevilacqua, M. Romano, Rendezvous Maneuvers of Multiple Spacecraft Using Differential Drag Under J2 Perturbation, Journal of Guidance, Control, and Dynamics 31 (2008 http://arc.aiaa.org/doi/10.2514/1.36362) 1595–1607.

[24] R. Bevilacqua, Analytical Guidance Solutions for Spacecraft Re-Phasing Based on Input Shaping, AIAA Journal of Guidance, Control, and Navigation 37 (2014 http://dx.doi.org/10.2514/1.g000008) 1042–1047.

[25] D. Guglielmo, R. Bevilacqua, Propellant-less Atmospheric Differential Drag LEo Spacecraft (PADDLES) Mission, in: Proceedings of the 2014 SmallSat Conference.

[26] Attitude Determination Control Systems, http://bluecanyontech.com/wp-content/uploads/2016/08/ADCS_F.pdf, ???? Blue Canyon Technologies.

[27] MAI-400 Specifications, http://maiaero.com/datasheets/MAI400_Specifications.pdf, ???? Maryland Aerospace, Inc.

[28] Attitude Determination and Control System, https://www.clyde.space/products/

51-attitude-determination-and-control-system, ???? Clyde Space, Ltd.

[29] M. Lovera, Magnetic Satellite Detumbling: The B-Dot Algorithm Revisited, in: Proceedings of the 2015 American Control Conference (ACC), pp. 1867–1872.

[30] P. C. Hughes, Spacecraft Attitude Dynamics, Courier Corporation, 2012.

[31] Dr. Fritz Faulhaber GMBH and Co. KG, Am1524-ww-ee, ???? https://www.micromo.com/media/pdfs/AM1524_FPS.PDF.

[32] Xiphos Systems Corporation, Q7 specifications, ???? http://xiphos.com/wp-content/uploads/2015/06/XTI-2001-2019-b_Q7_Spec_Sheet.pdf.

[33] D. Vallado, Fundamentals of Astrodynamics and Applications, Microcosm Press, Hawthorne, CA, 4 edition, 2013.

[34] D. A. Vallado, Fundamentals of Astrodynamics and Applications, volume 12, Springer Science & Business Media, 2001.

[35] S. R. Omar, J. M. Wersinger, Satellite Formation Control Using Differential Drag, in: Proceedings of the 53rd AIAA Aerospace Sciences Meeting, American Institute of Aeronautics and Astronautics, 2014.

[36] US Standard Atmosphere, National Aeronautics and Space Administration (NASA), 1976.

[37] J. Picone, A. Hedin, D. Drob, A. Aikin, Nrlmsise-00 Empirical Model of the Atmosphere: Statistical Comparisons and Scientific Issues, Journal of Geophysical Research: Space Physics 107 (2002). https://doi.org/10.1029/2002ja009430.

[38] K. Omar, M. Briggs, Simultaneous Orbital and Attitude Propagation of CubeSats in Low Earth Orbit, in: Proceedings of the 2016 SmallSat Conference.

[39] R. R. Bate, D. D. Mueller, J. E. White, Fundamentals of Astrodynamics, Dover Publications, New York, 1971.

[40] H. Curtis, Orbital Mechanics for Engineering Students, Elsevier, 2 edition, 2009.

[41] The Hysteresis Loop and Magnetic Properties, ???? https://www.nde-ed.org/EducationResources/CommunityCollege/MagParticle/Physics/HysteresisLoop.htm.

[42] E. Thébault, et al., International Geomagnetic Reference Field: The 12th Generation, Earth, Planets and Space 67 (2015). https://doi.org/10.1186/s40623-015-0228-9.

[43] T. W. Flatley, D. A. Henretty, A Magnetic Hysteresis Model, Technical Report, National Aeronautics and Space Administration (NASA), 1995. http://ntrs.nasa.gov/search.jsp?R=19950021380.

[44] Magnetic Moment of a Solenoid (Magnetic Moment of a Loop), http://www.whatitequals.com/content/magnetic-moment-solenoid-magnetic-moment-loop, ????

[45] S. Omar, An Inverse Dynamics Satellite Attitude Determination and Control System with Autonomous Calibration, in: Proceedings of the 2015 SmallSat Conference.

[46] R. R. Kumar, D. D. Mazanek, M. L. Heck, Simulation and Shuttle Hitchhiker Validation of Passive Satellite Aerostabilization, Journal of Spacecraft and Rockets 32 (1995) 806–811. http://arc.aiaa.org/doi/abs/10.2514/3.26688.

[47] J. Springmann, B. Kempke, J. Cutler, H. Bahcivan, Initial Flight Results of the RAX-2 Satellite, in: Proceedings of the 2012 SmallSat Conference.

[48] National Aeronautics and Space Administration Launch Services Program, Launch Services Program Program Level Dispenser and CubeSat Requirements Document, ???? https://www.nasa.gov/pdf/627972main_LSP-REQ-317_01A.pdf.